SUPPORTING INFORMATION

Spectroscopic Determination of Site-Selective Ligand Binding on Single Anisotropic Nanocrystals

Dong Le[1,2†], Wade Shipley[1,3†], Alexandria Do[1,3†], Liya Bi[1,4], Yufei Wang[1,3], Krista Balto[4], Rourav Basak[2] Hans A. Bechtel[5], Stephanie N. Gilbert Corder[5], Ilya Mazalov[3], Tesa Manto[2], Reno Sammons[2], Yutong She[3], Fiona Liang[3], Ganesh Raghavendran[3], Joshua S. Figueroa[4], Shaowei Li[1,4], Tod A. Pascal[1,3], Andrea R. Tao[1,3], Alex Frano[1,2]

[1]Material Science and Engineering Program, University of California San Diego, 9500 Gilman Drive, La Jolla, 92093, CA, USA.
[2]Department of Physics, University of California San Diego, 9500 Gilman Drive, La Jolla, 92093, CA, USA.
[3]Aiiso and Yufeng Li Family Department of Chemical and NanoEngineering, University of California San Diego, 9500 Gilman Drive, La Jolla, 92093, CA, USA.
[4]Department of Chemistry and Biochemistry, University of California San Diego, 9500 Gilman Drive, La Jolla, 92093, CA, USA.
[5]Advanced Light Source, Lawrence Berkeley National Laboratory, 1 Cyclotron Road, Berkeley, 94720, CA, USA.

[†]These authors contributed equally to this work.

E-mail: afrano@ucsd.edu

This PDF file includes:

1. Materials and Methods

1.1. Chemicals and Materials. Silver nitrate (≥99%), 1,5-pentanediol (PD, ≥97%), copper (II) chloride (≥98%), poly(vinylpyrrolidone) (PVP, average MW = 55 000 g/mol), Xylyl isocyanide (CNXylyl; Xylyl = 2,6-$Me_2C_6H_3$; 98%) were purchased from Sigma-Aldrich and used as received. Water used in experiments was obtained from a Millipore water purification system with a resistivity of 18.2 MΩ cm. The *m*-terphenyl isocyanide ligands $CNAr^{Mes2}$ (Ar^{Mes2} = 2,6-(2,4,6-$Me_3C_6H_2)_2C_6H_3$) were prepared as previously described. [1]

1.2. Synthesis and purification of PVP-grafted Silver Nanocubes (PVP-AgNCs). Silver nanocubes were synthesized through a polyol reaction as previously described. [2] In order to prepare the $AgNO_3$ precursor solution, 40 μL of 0.043 M $CuCl_2$ solution was combined with 0.20 g of $AgNO_3$ in 5 mL of 1,5-pentanediol. The mixture was then sonicated until the salt crystals were fully dissolved. Simultaneously, 0.20 g of PVP was dissolved in 10 mL of pentanediol. For the reaction solution, 10 mL of pentanediol was heated in a 50 mL glass round bottom flask and continuously stirred in an oil bath at 195°C. The $AgNO_3$ and PVP solutions were injected alternately into the flask at 500 μL/min rates and 320 μL/30 s, respectively, for five cycles. After injection, heating was ceased, and the solution was allowed to cool to room temperature. The resulting dispersion was filtered through membranes with 650, 450, and 220 nm pore sizes to remove nanowires and larger NPs. Finally, the filtered dispersion was centrifuged and redispersed to an optical density of 60 in chloroform, with a small amount of ethanol added for stabilization.

1.3. Synthesis of $CNAr^{Mes2}$-AgNCs and CNXylyl-AgNCs. To perform the ligand exchange (LE) process, $CNAr^{Mes2}$ or CNXylyl isocyanide was added to 1 mL of AgNC dispersion to achieve a final concentration of 50 μM. The mixture was reactivated for 4 hours to complete the ligand exchange. After the reaction, the dispersion was washed twice to remove excess ligands. The resulting sediment was then redispersed in chloroform for use in further experiments.

1.4. Nanocrystal Characterizations. Scanning electron microscopy (SEM) was conducted using an FEI Apreo SEM at an accelerating voltage of 5 kV. UV–visible absorption measurements were performed on Cary 50/60 UV-Vis spectrophotometer. Dynamic Light Scattering (DLS) was performed using the Malvern Instruments Zetasizer Nano. Raman measurements were performed with a Renishaw micro-Raman spectrometer (Renishaw Invia) coupled with a Leica microscope, utilizing a 50× objective (Leica N-plan) and covering the range of 800 −2400cm^{-1}. The excitation source was a 532 nm wavelength generated by a 50 mW Arlon laser. Far-field ATR-FTIR measurements were employed to detect the properties of both bound and unbound isocyanide groups on silver. Atomic Force Microscopy (AFM) topography and phase images were taken with a Park Systems NX20 atomic force microscope with a 4XC-NN tip produced by MikroMasch. Due to contrasts in surface topography with sharp vertical nanocube sidewalls and flat nanocube surfaces, some ringing artifacts were observed on the nanocube sidewalls. This was rectified with adaptive scanning and some limited ASF closing filters applied to the sidewalls in Gwyddion 2.62. The tip oscillation amplitude was kept between 45 and 55 nm to balance, optimize tracking and maintain sensitive phase contrast. All AFM image analysis was performed in Gwyddion. Small-angle X-ray Scattering (SAXS) experiments was conducted using the Xeuss 3.0 instrument, which consists of the Cu based Genix3D μ-source X-ray beam with an Eiger 2R

1M 2D detector from Dectris. Each sample was diluted in ethanol in the standard 1.5-1.8 x 90 mm capillary tubes and were ran for 25 minutes each under standard configuration in ESAXS mode (SDD of 1800 mm). The standard atmospheric caps were installed on the Xeuss. Aliquots were taken from the center of the vials after being shaken to try and get a representative population. Data is processed using the XSACCT software from Xenocs.

1.5. Sample preparation for SINS measurement. Functionalized AgNCs in chloroform were drop-cast onto the water surface in a glass petri dish. Once the chloroform evaporated, the petri dish was covered, allowing the monolayer to assemble over several hours. This assembled monolayer was then transferred onto the surface of a gold substrate – Au(111) – by vertically dip-coating it. After this process, the sample was ready for SINS measurement.

1.6. Synchrotron infrared nanospectroscopy (SINS). SINS measurements were conducted at beamline 5.4 of the Advanced Light Source at Lawrence Berkeley National Laboratory. Infrared light was focused onto the apex of a Pt-coated AFM tip (NCH-Pt by Nanosensors) within a modified AFM system (Innova, Bruker). [3] Due to the nonlinear dependency of the near-field scattered signal on the tip-sample distance, tip oscillation induced higher harmonics $(n\omega)$ in the scattered signal. [3] The high harmonics frequency of 2ω was detected using a lock-in amplifier to isolate the near-field signal from the far-field background. [3] A modified commercial FTIR spectrometer (Nicolet 6700, Thermo Scientific) was used to collect the infrared nanospectroscopy measurements. After obtaining AFM topography images of the sample surface, IR nanospectroscopy point measurements were performed at selected locations. The complex-valued near-field spectrum was derived from the Fourier transform of the interferogram, with the real (Re(v)) and imaginary (Im(v)) components represented as spectral amplitude $A(v)$ and phase $\phi(v)$, respectively. Near-field spectra were reported in the form of a normalized scattering phase, $\phi(v) = \phi_{sample}(v) - \phi_{reference}(v)$, using the bare Au-coated glass substrate as the reference. Spectral processing was performed using custom software developed at the beamline's end station. IR nanospectroscopy measurements were performed at multiple sites across the surfaces of several nanoparticles in each sample. At each location, spectra were collected repeatedly and averaged to improve the signal-to-noise ratio. Prior to acquiring each IR spectrum, the sample was allowed to reach thermal equilibrium, ensuring thermal drift was less than 5 nm/min. The IR signal was continuously monitored during acquisition to maintain precise tip positioning and measurement accuracy.

1.7. Scanning tunneling microscopy (STM) and inelastic electron tunneling spectroscopy (STM-IETS). The STM and STM-IETS experiments were performed using a customized CreaTec low-temperature STM operating at approximately 5 K and a base pressure of less than 1×10^{-10} Torr. The Ag(111) substrate was cleaned by successive cycles of Ar^+ sputtering and thermal annealing. The electrochemically etched W tip was cleaned and sharpened by Ar^+ sputtering and thermal annealing, followed by conditioning through repeated poking on the Ag(111) surface until single-molecule resolution was achieved. The thermal stability of $CNAr^{Mes2}$ has been examined. [4] We dosed the $CNAr^{Mes2}$ ligands onto the clean Ag(111) surface at 5 K via thermal sublimation using a homemade Knudsen cell evaporator within the vacuum chamber. To promote surface diffusion of $CNAr^{Mes2}$ ligands, the sample was gradually warmed from 5 K to room temperature by removing it from the STM cryostat. Subsequently, the sample was cooled back down to 5 K for examination. Topographic images were acquired in constant current mode by recording the ***z***-

position with feedback engaged and processed using Gwyddion. [5] The d^2I/dV^2 spectra were obtained by recording the second harmonic output of a lock-in amplifier while sweeping the bias voltage. A modulation of 3 mV (root mean square) at a frequency of 377 Hz was applied to the sample bias, with feedback turned off during bias sweeping.

2. Computational Details

2.1. DFT Calculations. To calculate the binding energies of $CNAr^{Mes2}$ and CNXylyl to Ag surfaces, Density Functional Theory (DFT) calculations were performed using the Quantum Espresso (QE) package [6], using the PBE exchange correlation functional [7] and the ultrasoft pseudopotentials of Dal Corso *et al.* [8] The wavefunction kinetic energy cutoff was set to 60 (Ry) and a convergence tolerance of 1E-08 Ry, while the cutoff for the charge density was set to 480 (Ry). A 15x15x15 K-point grid was used to efficiently sample the Brillouin zone. To capture the interactions of the isocyanide ligands with Ag, the (100) and (111) surfaces were constructed, with a minimum of four layers of Ag atoms and a vacuum layer of at least 40 Å. Self-Consistent Field (SCF) calculations were performed on the isolated ligand, bulk Ag, and each of the slab geometries. The total energies of the $CNAr^{Mes2}$ and CNXylyl ligands on each of the Ag slabs were obtained, with the distance between the isocyanide C and the slab surface were set to distances ranging between 2 - 10 Å in 1 Å increments, followed by a finer scale of 0.1 Å increments about the energy minima. The binding energy was calculated as:

$$E_{binding} = E_{slab|ligand} - E_{slab} - E_{ligand}$$

2.2. MD Simulations. A 30x30x30 (Å) silver nanocube with exposed (100) faces, consisting of 2457 atoms, was placed in the center of a 100x100x100 $Å^3$ box. Ninety-eight $CNAr^{Mes2}$ and CNXylyl ligands were added, then the entire system was solvated with 7,300 chloroform molecules using the Packmol package. [9]

Classical molecular dynamics (MD) simulations were performed using the LAMMPS simulation engine [10]. The Ag atoms that constitute the nanocube were described using the Embedded Atom/Finnis-Sinclair Method, with pairwise interactions developed Ackland and coworkers [11]. The $CNAr^{Mes2}$ and CNXylyl ligands were primarily described with the GAFF force field [12], while the C≡N bond stretch and ring torsions were described using the QM-corrected parameters obtained in our previous work. [13] The chloroform molecules were described using the parameters developed by Kamanth *et al.* [14] The Ag – ligand van der Waals (vdW) interactions were obtained from Lorentz-Berthelot [15] mixing rules, assuming the Ag van der Waals parameters in UFF. [16]

The van der Waals and real space coulomb cutoffs in the MD simulations were 10 Å. A cubic spline was applied to the van der Waals interactions to ensure smooth convergence and vanishing energies and forces at the cutoff (inner cutoff distance of 9Å). The reciprocal space coulomb interactions were computed with a particle-particle-particle-mesh solver, with an error tolerance of 10^{-6}. [17] Each MD simulation was initiated with 500 conjugated gradient steps, followed by gradual heating to 5K using 0.5 ns (500,000 steps with an integration timestep of 1 fs) dynamics in the canonical ensemble (NVT – constant number of particles N, volume V and temperature T = 298.15 K). A Nose-Hoover thermostat was used with a temperature relaxation window of 100 fs. The time-reversible measure-preserving Verlet integrators derived by Tuckerman *et al*. [18] was applied for the time integration. After density equilibration, the system was simulated in the NVT ensemble for at least 5 ns of NVT dynamics.

2.3. Simulated Raman Spectra. To observe the C≡N stretching mode, simulated Raman spectroscopy was done using a modified form of the 2-Phase Thermodynamics code (2PT). [19] After 5 ns of NVT dynamics, sampling groups were obtained by identifying isocyanide ligands that were either freely floating in solution or bound to a corner, or planar site. Next, the 2PT trajectory was generated by subjecting the simulated systems to an additional 200 ps of NVT dynamics, with sampling occurring every 4 fs.

The vibrational power spectrum $\alpha_{\omega}^{V_{vib}}$ was obtained from the generated trajectory file:

$$\alpha_{\omega}^{V_{vib}} = \int_{-\infty}^{\infty} dt \, \langle V_{vib}(t).V_{vib}(0)\rangle \exp(i\omega t)$$

Where t is time, ω is frequency, V_{vib} is the vibrational component of the velocity of the species.

The IR spectra of neutral species (α_{ω}^{IR}) was generated from the Fast Fourier Transform (FFT) of the time correlation of molecular dipole moments (D_{mol}) :

$$D_{mol} = \sum_{1}^{n} q.\vec{r}$$

Where 'n' is the number of atoms in a molecule, 'q' and '$\vec{r}$' are charge and position vector of the atom, respectively.

$$\alpha_{\omega}^{IR} = \frac{2\pi\omega(1-\exp(-\beta\hbar\omega))}{3\hbar c V \mu_{\omega}} * \int_{-\infty}^{\infty} dt \, \langle D_{mol}(t).D_{mol}(0)\rangle \exp(i\omega t)$$

Where $\hbar$ is reduced Planck's constant, c is speed of light, V is the volume of the species under consideration, μ_{ω} is the refractive index of the medium at frequency ω and $\beta = 1/kT$, T being the temperature and k the Boltzmann constant. μ_{ω} is considered constant for simplicity.

The "unscaled" Raman spectra (α_{ω}^{Raman}) was generated by subtracting the IR spectrum from the vibration power spectrum of the species:

$$\alpha_{\omega}^{Raman} = \alpha_{\omega}^{V_{vib}} - 1 * \alpha_{\omega}^{IR}$$

3. Supporting Figures

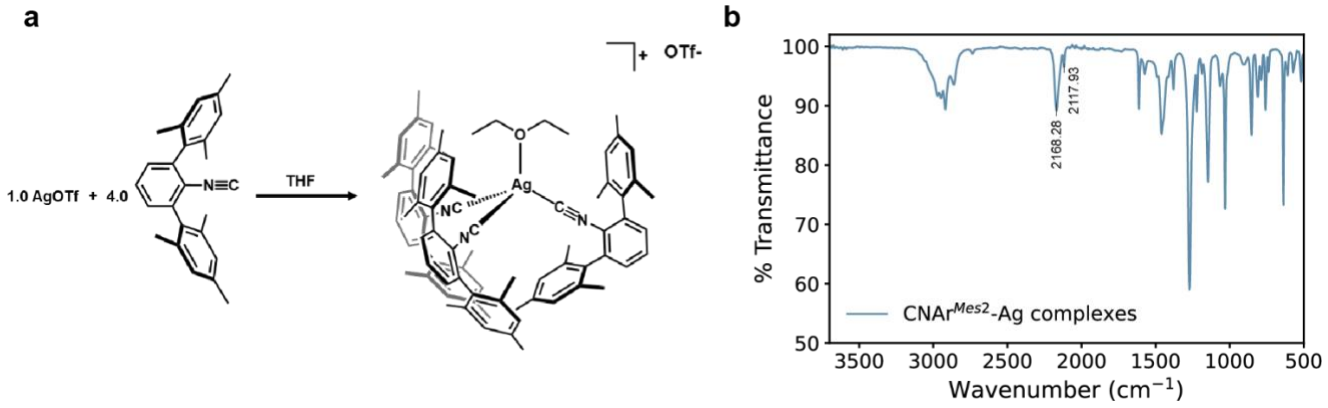

Figure S1. (a) Synthetic route to [Ag(Et_2O)($CNAr^{Mes2}$)$_3$]OTf. (b) ATR-IR spectrum of [Ag(Et_2O)($CNAr^{Mes2}$)$_3$]OTf from (a). Isocyanide stretching frequency of bound dimesityl phenyl isocyanide ($CNAr^{Mes2}$) to Ag is $\nu_{CN} \sim 2168\ cm^{-1}$. Free $CNAr^{Mes2}$ is observed at $\nu_{CN} \sim 2118\ cm^{-1}$.

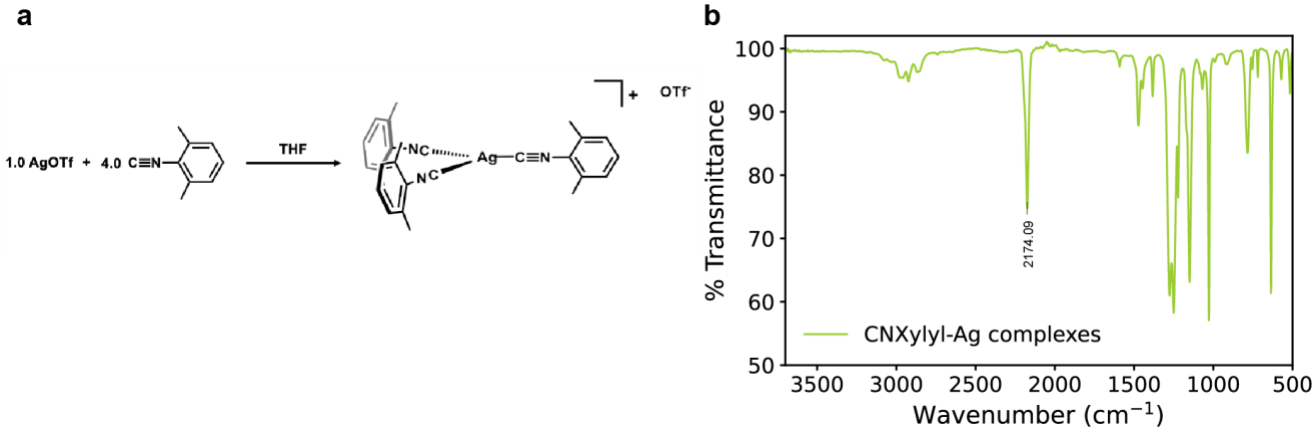

Figure S2. (a) Synthetic route to [Ag($CNXylyl$)$_3$]OTf. (b) ATR-IR spectrum of the product of AgOTf and *m*-Xylyl isocyanide (CNXylyl) from (a). Isocyanide stretching frequency of bound CNXylyl isocyanide to Ag is $\nu_{CN} \sim 2174\ cm^{-1}$.

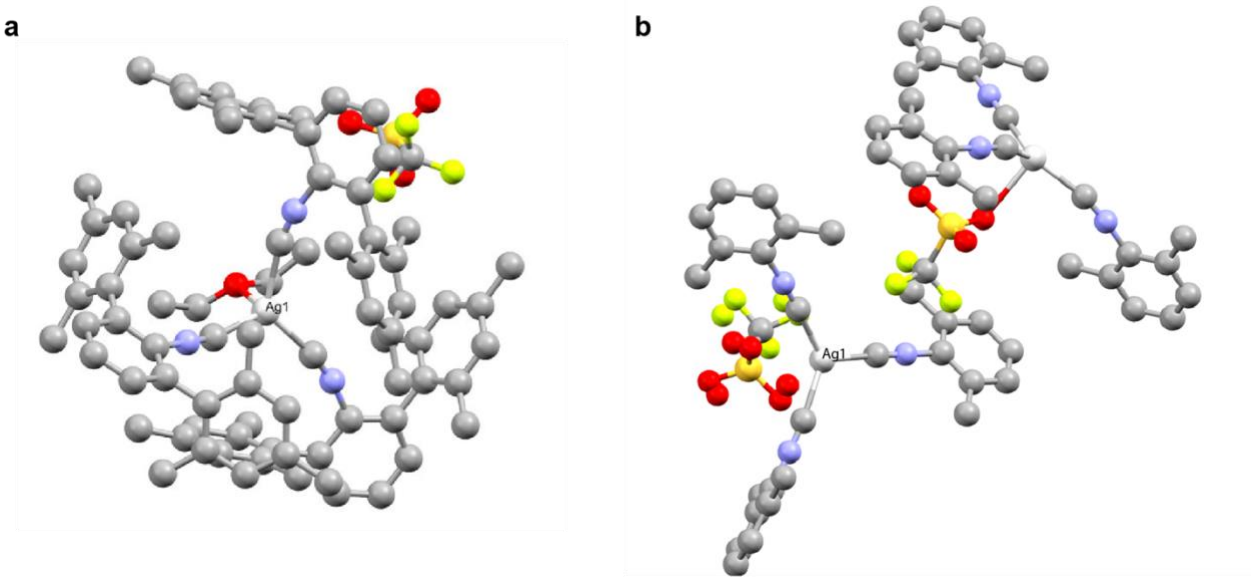

Figure S3. X-ray crystal structure along the crystallographic *b* axis of (a) $[Ag(Et_2O)(CNAr^{Mes2})_3]OTf$ and of (b) $[Ag(CNXyl)_3]OTf$. Hydrogens are omitted for clarity.

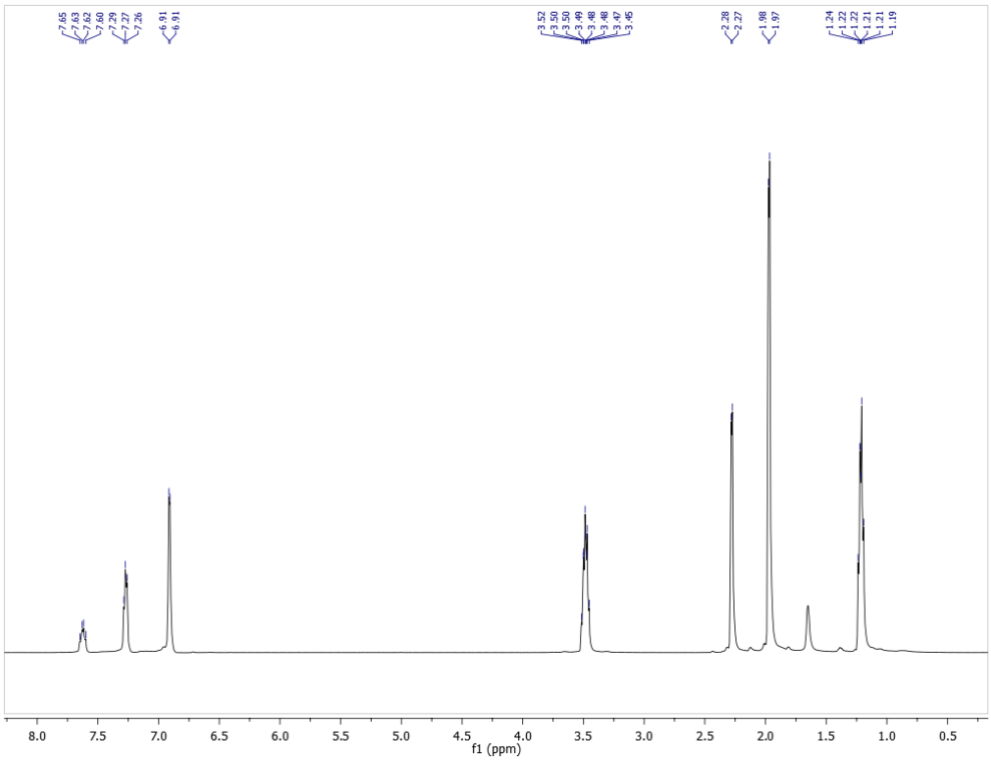

Figure S4. ^{1}H-NMR spectrum of [Ag(Et_2O)($CNAr^{Mes2}$)$_3$]OTf in $CDCl_3$. Free $CNAr^{Mes2}$ observed in the spectrum.

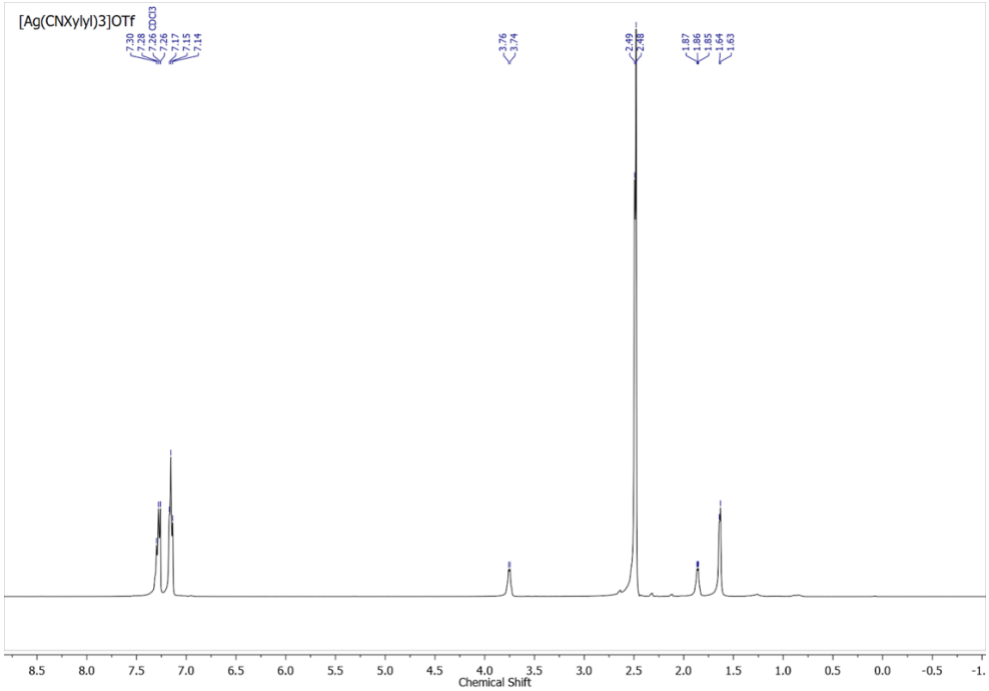

Figure S5. ^{1}H-NMR spectrum of [Ag(CNXylyl)$_3$]OTf in $CDCl_3$.

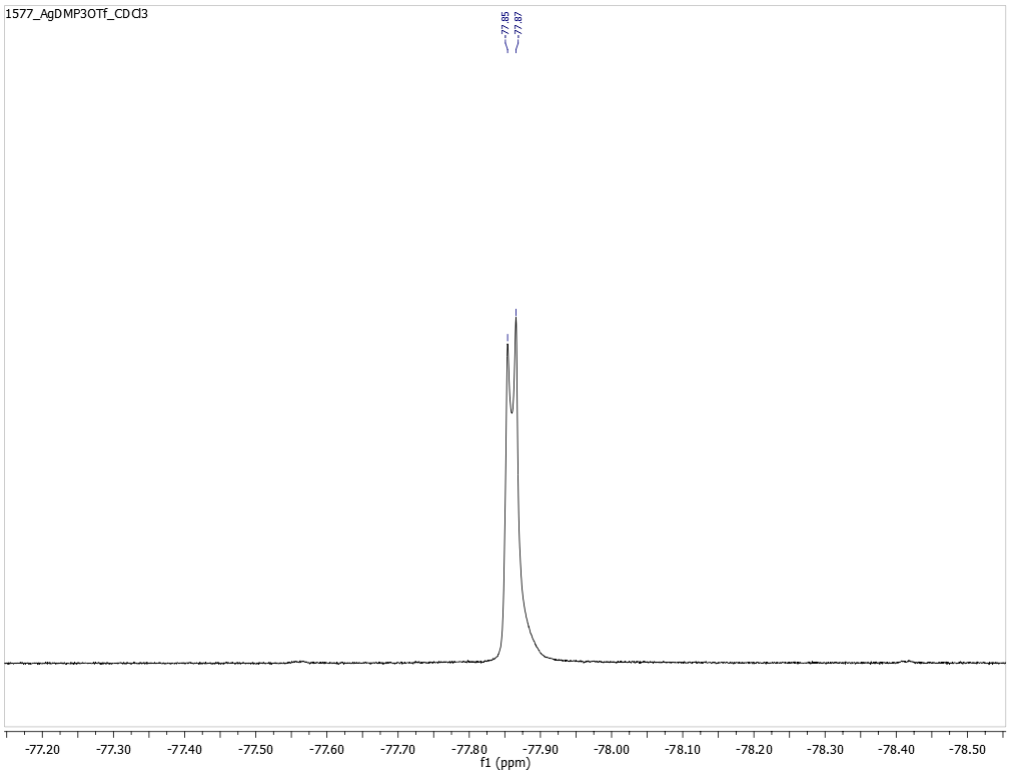

Figure S6. ^{19}F-NMR spectrum of $[Ag(Et_2O)(CNAr^{Mes2})_3]OTf$ in $CDCl_3$.

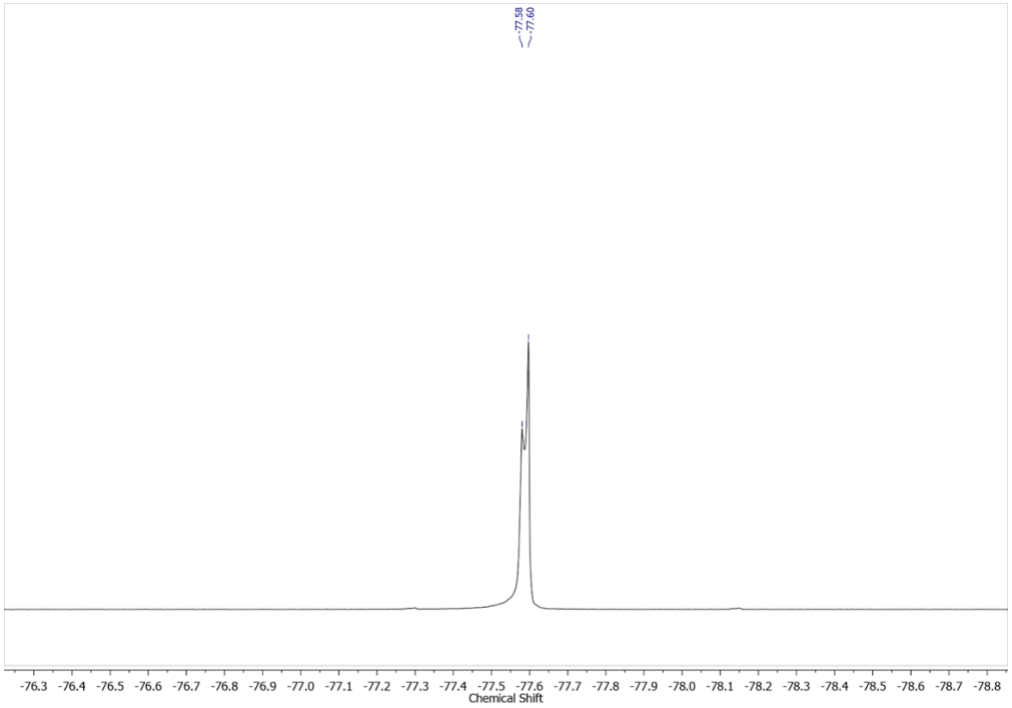

Figure S7. ^{19}F-NMR spectrum of $[Ag(CNXyl)_3]OTf$ in $CDCl_3$.

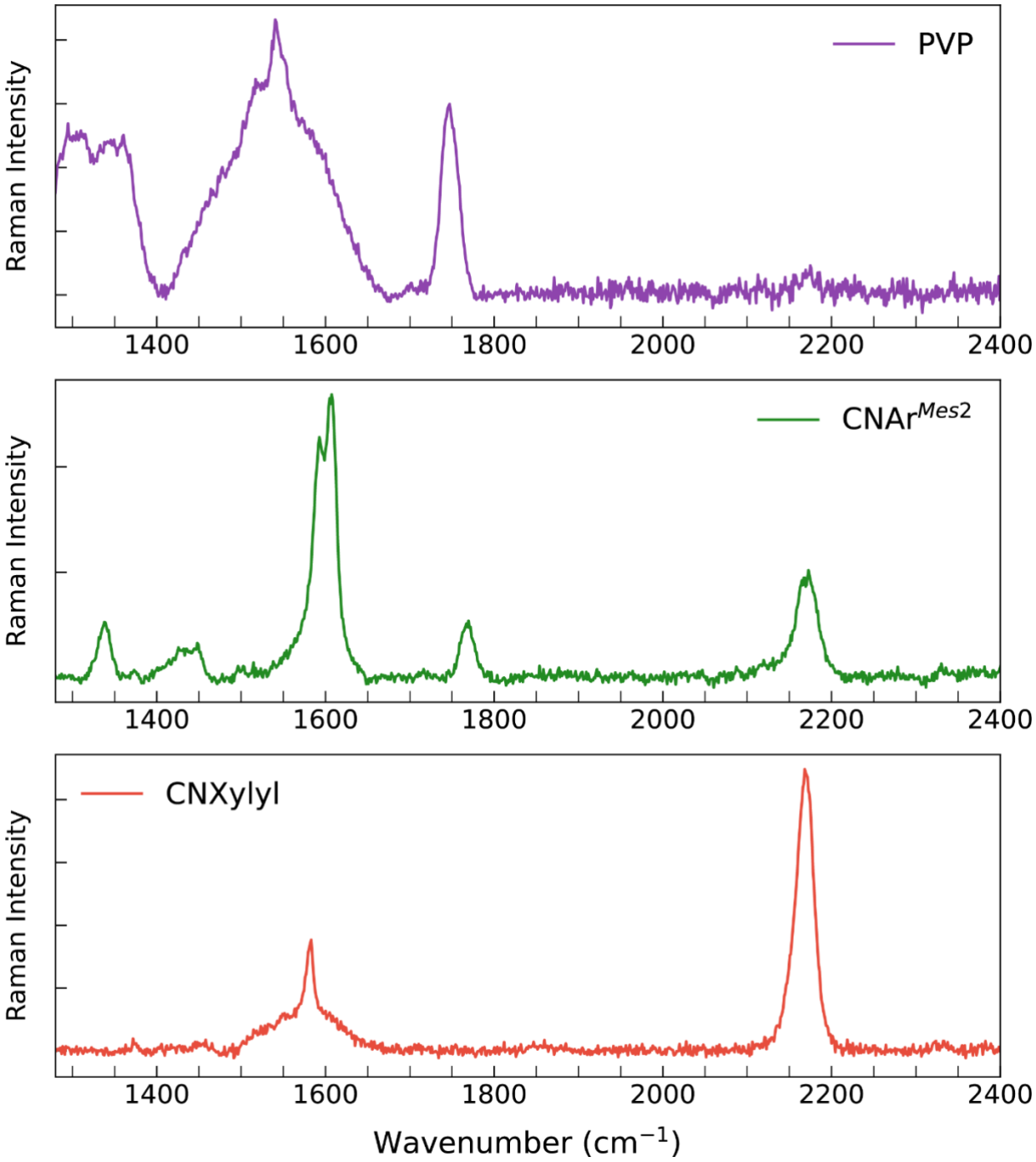

Figure S8. SERS spectra of 80 nm AgNCs before (PVP-AgNCs) and after (CNAr^{Mes2}-AgNCs and CNXylyl-AgNCs) the LE process. Binding of isocyanide ligands CNAr^{Mes2} and CNXylyl to AgNCs is indicated by the $\nu(C \equiv N)$ stretching at ~ 2177 cm^{-1}. Peaks around 1600 cm^{-1} and 1760 cm^{-1} are assigned for $C = O$ stretching.

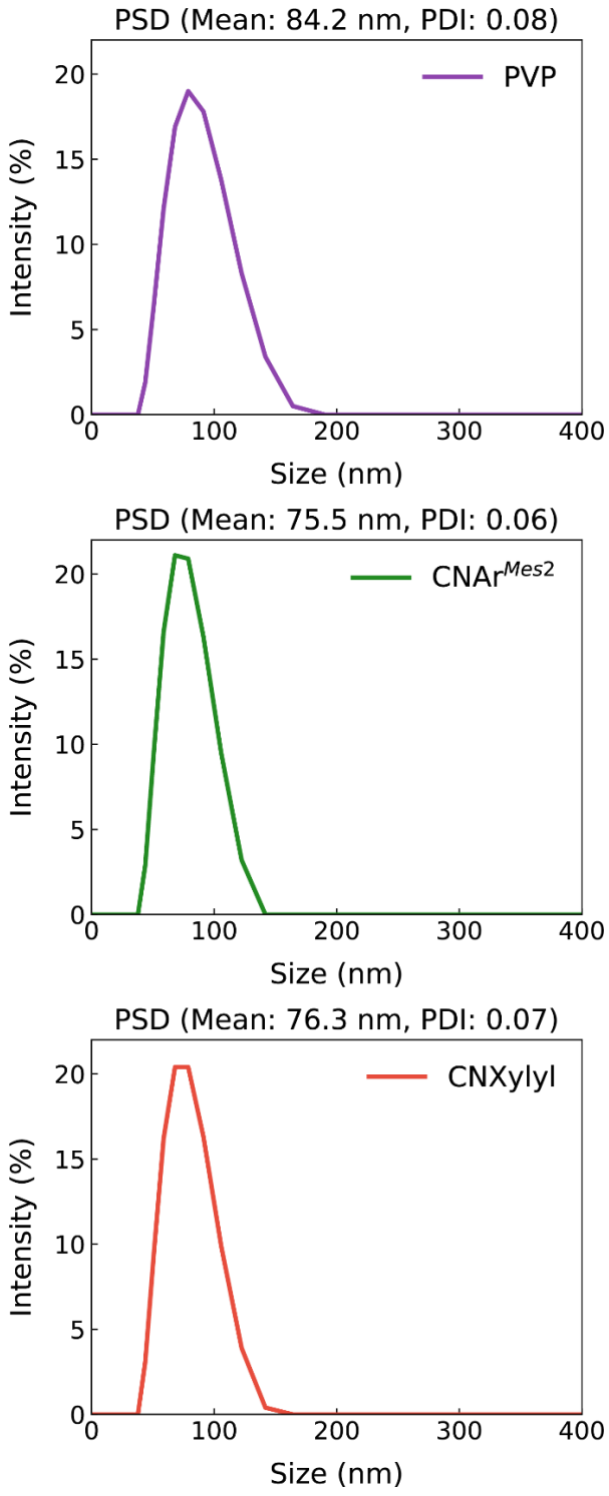

Figure S9. Dynamic Light Scattering (DLS) plot of AgNCs before (PVP-AgNCs) and after (CNAr^{Mes2}-AgNCs and CNXylyl-AgNCs) the ligand exchange (LE) process. The plots show the hydrodynamic diameter and polydispersity index (PDI) for nanoparticles diluted in chloroform, indicating monodisperse systems.

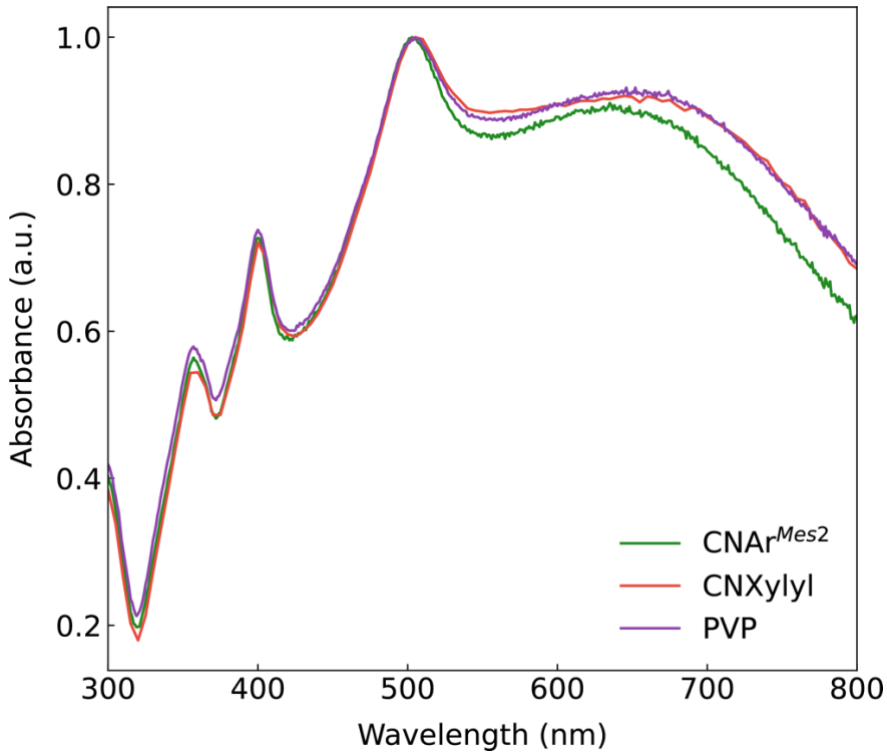

Figure S10. Ultraviolet-visible (UV-Vis) absorbance spectra of samples *before* (PVP-AgNCs) and *after* (CNAr^{Mes2}-AgNCs and CNXylyl-AgNCs) the ligand exchange (LE) process.

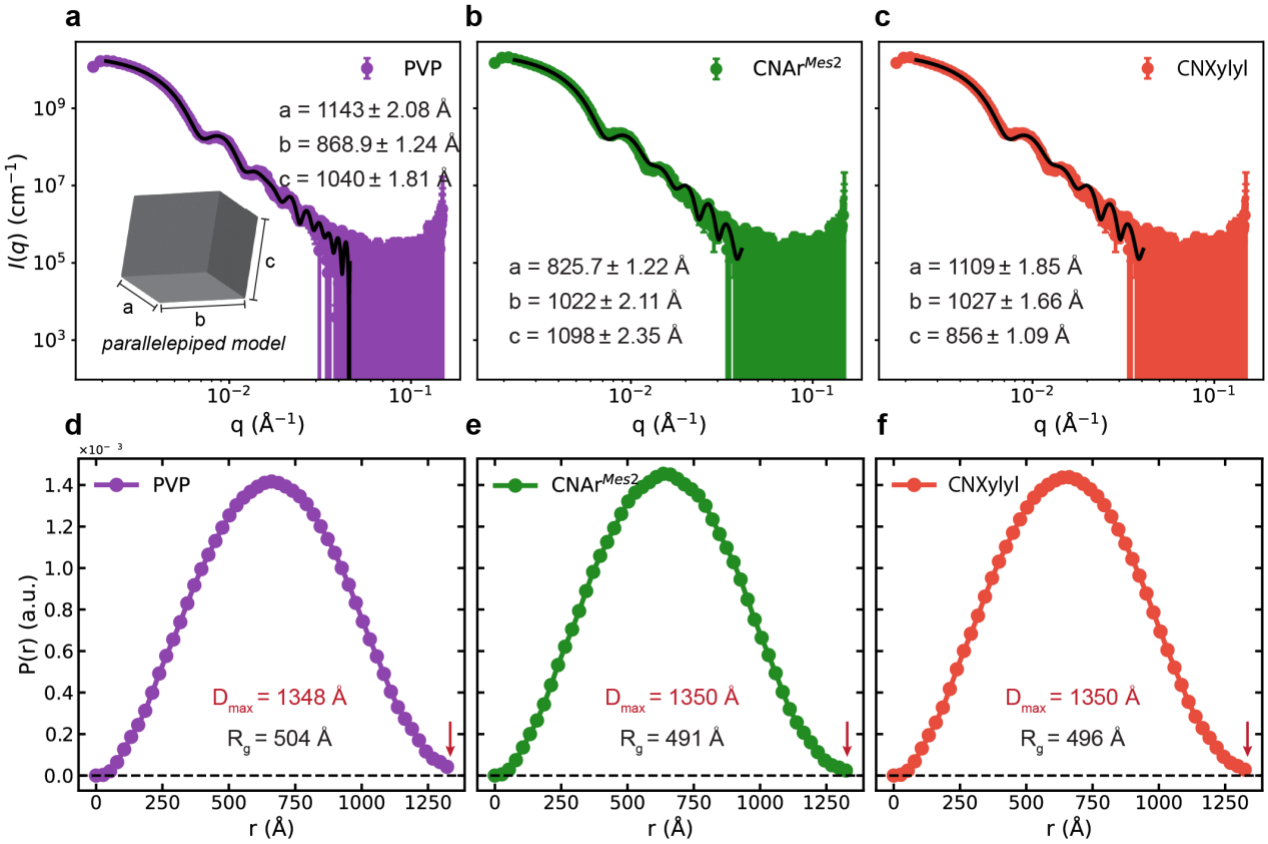

Figure S11. SAXS characterization of AgNCs before and after ligand exchange. (a) SAXS profile of PVP-AgNCs diluted in ethanol prior to ligand exchange process. (b-c) SAXS profiles of Ag nanocubes after exchange with $CNAr^{Mes2}$ and CNXylyl ligands, respectively, also measured in ethanol. Each dataset (colored symbols) is fitted with a parallelepiped model (black lines), which captures the overall particle shape and dimensions (a-c). The fits show good agreement with the experimental data, indicating well-defined nanocube geometry across all samples. The inset in (a) illustrates the parallelepiped model used for fitting. (d–f) Corresponding pair-distance distribution functions, *P(r)*, show comparable maximum particle dimensions (D_{max} ≈ 1350 Å) across all three samples. Slight differences in the radius of gyration, R_g, reflect subtle variations in overall shape and surface structure following ligand exchange. Compared to the PVP-grafted sample, $CNAr^{Mes2}$-AgNCs and CNXylyl-AgNCs exhibit slightly reduced R_g, possibly due to differences in ligand shell organization or packing density.

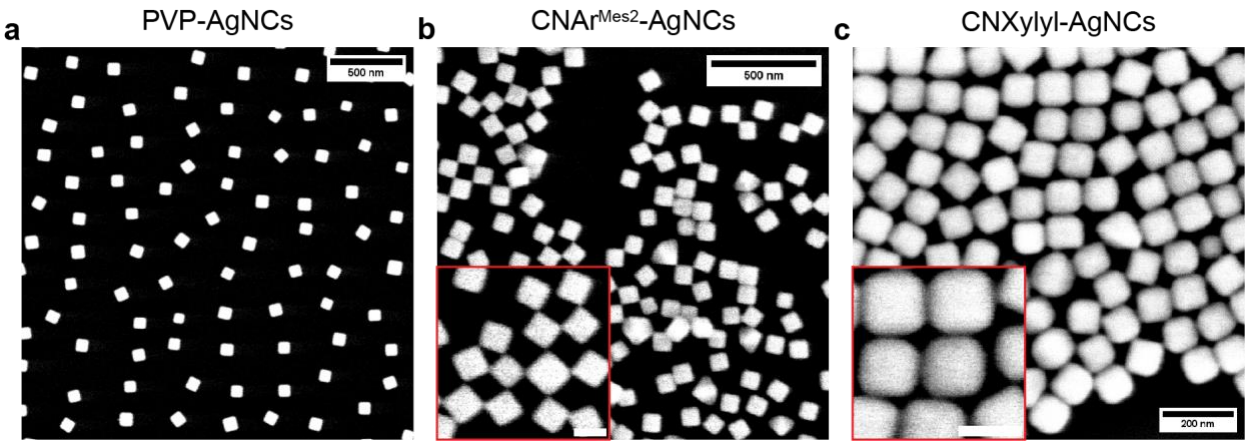

Figure S12. SEM images of samples *before* (a) PVP-AgNCs and after (b) CNAr^{Mes2}-AgNCs, (c) CNXylyl-AgNCs the LE process. Different ligands result in different final assembled structural outcome. Inset scale bar 100 nm.

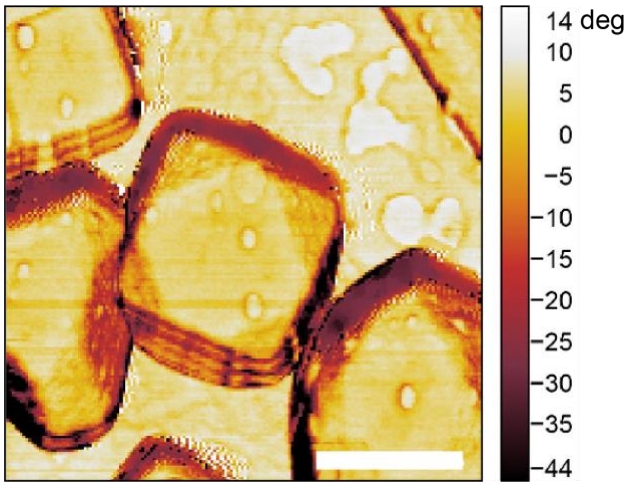

Figure S13. AFM image showing the cuboid shape with a steep edge near the corner of the cube. Scale bar, 100 nm.

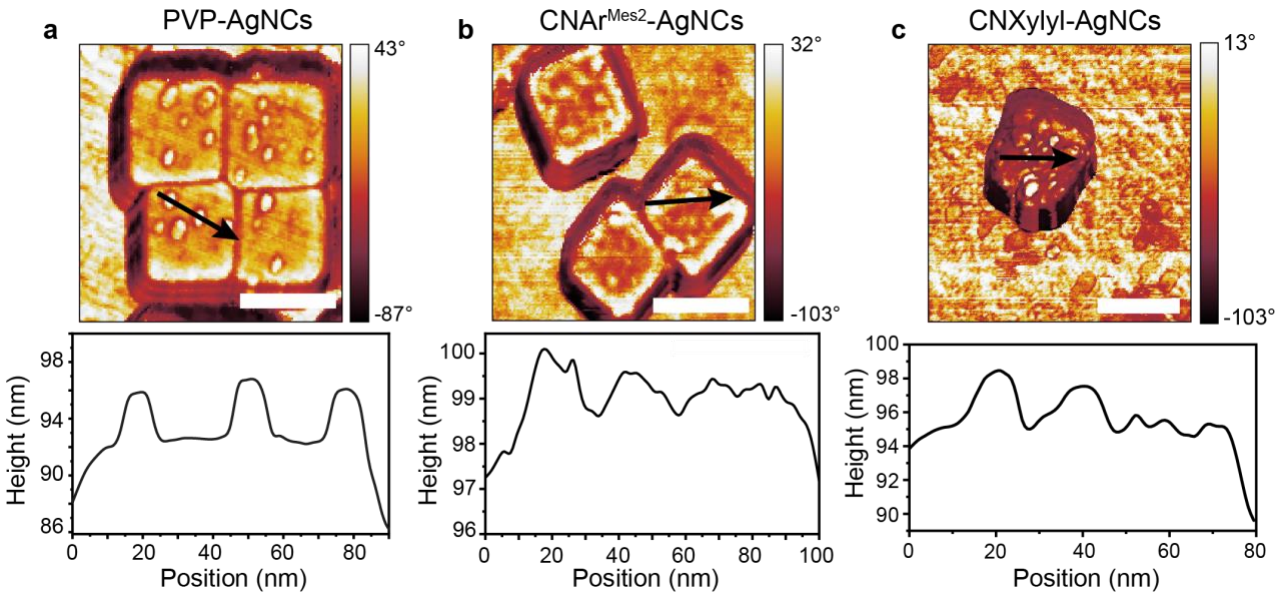

Figure S14. AFM images comparing changes in surface morphology of samples before and after the LE exchange process. PVP grafted AgNCs shown in (a) were expected to have even surface coverage, with each molecule bound to the AgNC surface at several points. Some bumps on the surface are visible, with a topographic line profile shown from the region marked with an arrow. These could correspond to a drying artifact of the PVP graft layer with single chains adopting a more clustered configuration. In comparison, the phase images for the CNAr^{Mes2}-AgNCs and CNXylyl-AgNCs were shown in (b) and (c), respectively. The surfaces of CNAr^{Mes2}-AgNCs were rougher but with fewer large clusters. This change suggests the presence of free and bound ligands covering the surface of the cube. For CNXyl-AgNCs, the surface of the nanocube has many clusters of various sizes with few smooth surface regions. This surface likely consists of both PVP and CNXylyl clusters, with the PVP potentially corresponding to the larger clusters. This is consistent with CNXylyl modifications on the faces and corners of the AgNCs. Scale bar, 100 nm.

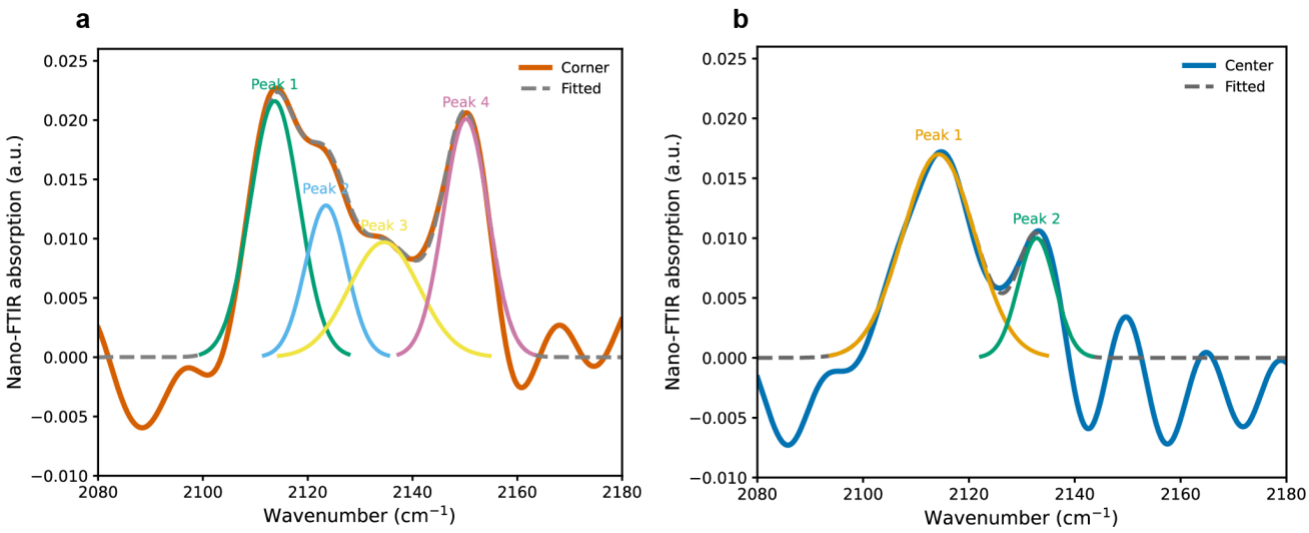

Figure S15. Gaussian peak deconvolution of the C≡N stretching region from SINS spectra for $CNAr^{Mes2}$-AgNC sample. (a) Corner and (b) center spectra were fitted using Gaussian functions to resolve overlapping vibrational features. The dominant peaks at ν_s(C≡N) = 2114 cm^{-1}, (Peak 1) observed in both spectra, are attributed to physisorbed $CNAr^{Mes2}$ ligands. A distinct additional peak at ν_s(Ag–C≡N) = 2150 cm^{-1} (peak 4) is present only in the corner spectrum, consistent with predicted chemisorbed $CNAr^{Mes2}$ at low-coordinate sites. Peaks of lower intensity could arise from intermolecular interactions or orientation-induced coupling with the near-field, but further theoretical analysis is required to confirm their origin. These results support the conclusion that ligand binding preferentially occurs at corner sites on the nanocube surface after ligand exchange.

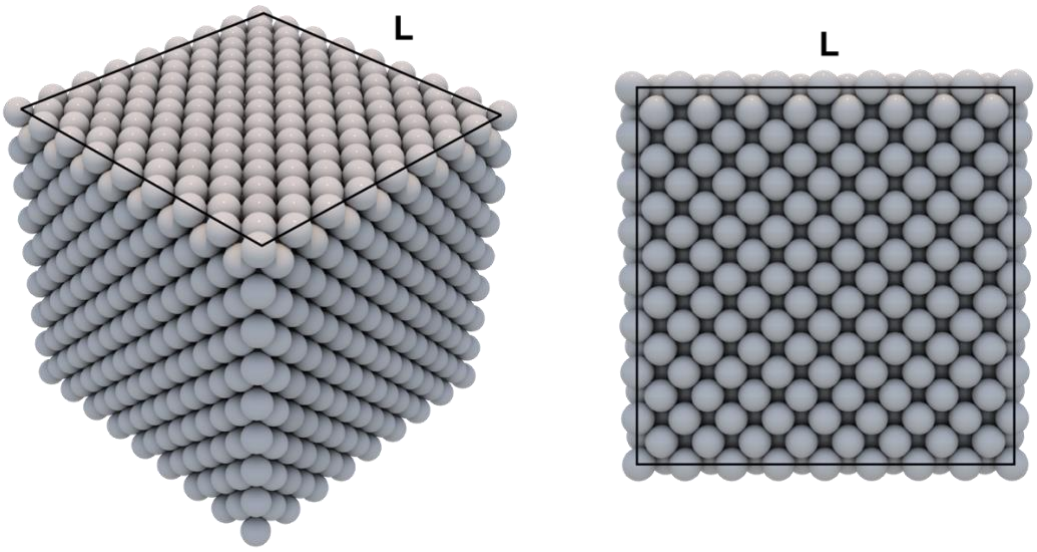

Figure S16. Initial structure of AgNCs used in MD simulation. The edge length, L, is 32.68 Å bounded by Ag(100) and Ag(111) facets.

4. Supporting Tables

Simulated *v*	CNAr^{Mes2}	CNXylyl
Corner Site	2170 cm^{-1}	2172 cm^{-1}
Planar Site	2165 cm^{-1}	2171 cm^{-1}
In Solution	2148 cm^{-1}	2148 cm^{-1}

Table S1. Simulated C≡N stretching frequencies for Ag-bound and free-floating isocyanide ligands.

5. References

1. Brian J. Fox et al. “Solution Behavior and Structural Properties of Cu(I) Complexes Featuring m-Terphenyl Isocyanides”. In: *Inorganic Chemistry* 47.19 (Oct. 2008). Publisher: American Chemical Society, pp. 9010–9020. issn: 0020-1669.
2. Andrea Tao, Prasert Sinsermsuksakul, and Peidong Yang. “Polyhedral Silver Nanocrystals with Distinct Scattering Signatures”. In: *Angewandte Chemie International Edition* 45.28 (2006). eprint: https://onlinelibrary.wiley.com/doi/pdf/10.1002/anie.200601277, pp. 4597–4601. issn: 1521-3773.
3. Liya Bi et al. “Molecular-Scale Visualization of Steric Effects of Ligand Binding to Reconstructed Au(111) Surfaces”. In: *Journal of the American Chemical Society* 146.17 (May 2024). Publisher: American Chemical Society, pp. 11764– 11772. issn: 0002-7863.
4. David Ne˘cas and Petr Klapetek. “Gwyddion: an open-source software for SPM data analysis”. en. In: *Open Physics* 10.1 (Feb. 2012). Publisher: De Gruyter Open Access Section: Open Physics, pp. 181–188. issn: 2391-5471.
5. Hans A. Bechtel et al. “Synchrotron infrared nano-spectroscopy and -imaging”. en. In: *Surface Science Reports* 75.3 (Aug. 2020), p. 100493. issn: 01675729.
6. Giannozzi, P.; Andreussi, O.; Brumme, T.; Bunau, O.; Buongiorno Nardelli, M.; Calandra, M.; Car, R.; Cavazzoni, C.; Ceresoli, D.; Cococcioni, M.; Colonna, N.; Carnimeo, I.; Dal Corso, A.; de Gironcoli, S.; Delugas, P.; DiStasio, R. A.; Ferretti, A.; Floris, A.; Fratesi, G.; Fugallo, G.; Gebauer, R.; Gerstmann, U.; Giustino, F.; Gorni, T.; Jia, J.; Kawamura, M.; Ko, H.-Y.; Kokalj, A.; Küçükbenli, E.; Lazzeri, M.; Marsili, M.; Marzari, N.; Mauri, F.; Nguyen, N. L.; Nguyen, H.-V.; Otero-de-la-Roza, A.; Paulatto, L.; Poncé, S.; Rocca, D.; Sabatini, R.; Santra, B.; Schlipf, M.; Seitsonen, A. P.; Smogunov, A.; Timrov, I.; Thonhauser, T.; Umari, P.; Vast, N.; Wu, X.; Baroni, S. Advanced Capabilities for Materials Modelling with Quantum Espresso. *Journal of Physics: Condensed Matter* **2017**, *29* (46), 465901.
7. Perdew, J. P.; Burke, K.; Ernzerhof, M. Generalized Gradient Approximation Made Simple. *Physical Review Letters* **1996**, *77* (18), 3865–3868.
8. Dal Corso, A. Pseudopotentials Periodic Table: From H to Pu. *Computational Materials Science* **2014**, *95*, 337–350.
9. L. Martínez, R. Andrade, E. G. Birgin, J. M. Martínez. Packmol: A package for building initial configurations for molecular dynamics simulations. *Journal of Computational Chemistry*, 30(13):2157-2164, 2009.
10. Thompson, A. P.; Aktulga, H. M.; Berger, R.; Bolintineanu, D. S.; Brown, W. M.; Crozier, P. S.; in ’t Veld, P. J.; Kohlmeyer, A.; Moore, S. G.; Nguyen, T. D.; Shan, R.; Stevens, M. J.; Tranchida, J.; Trott, C.; Plimpton, S. J. LAMMPS - a Flexible Simulation Tool for Particle-Based Materials Modeling at the Atomic, Meso, and Continuum Scales. *Computer Physics Communications* **2022**, *271*, 108171.
11. Ackland, G. J.; Tichy, G.; Vitek, V.; Finnis, M. W. Simple *n*-Body Potentials for the Noble Metals and Nickel. *Philosophical Magazine A* **1987**, *56* (6), 735–756.
12. Wang, J.; Wolf, R. M.; Caldwell, J. W.; Kollman, P. A.; Case, D. A. Development and Testing of a General Amber Force Field. *Journal of Computational Chemistry* **2004**, *25* (9), 1157–1174.
13. Wang, Y.; Chen, A. A.; Balto, K. P.; Xie, Y.; Figueroa, J. S.; Pascal, T. A.; Tao, A. R. Curvature-Selective Nanocrystal Surface Ligation Using Sterically-Encumbered Metal-Coordinating Ligands. *ACS Nano* **2022**, *16* (8), 12747–12754.

14. Kamath, G.; Georgiev, G.; Potoff, J. J. Molecular Modeling of Phase Behavior and Microstructure of Acetone−chloroform−methanol Binary Mixtures. *The Journal of Physical Chemistry B* **2005**, *109* (41), 19463–19473.
15. Lorentz, H. A. Ueber die Anwendung des Satzes vom Virial in der kinetischen Theorie der Gase. *Annalen der Physik* **248**, 127-136.
16. Rappe, A. K., Casewit, C. J., Colwell, K. S., Goddard, W. A., III & Skiff, W. M. UFF, a full periodic table force field for molecular mechanics and molecular dynamics simulations. *Journal of the American Chemical Society* **114**, 10024-10035, (1992).
17. Hockney, R. W. & Eastwood, J. W. *Computer simulation using particles*. (Adam Hilger, 1989).
18. Tuckerman, M. E., Alejandre, J., López-Rendón, R., Jochim, A. L. & Martyna, G. J. A Liouville-operator derived measure-preserving integrator for molecular dynamics simulations in the isothermal–isobaric ensemble. *Journal of Physics A: Mathematical and General* **39**, 5629, (2006).
19. Lin, S.-T.; Blanco, M.; Goddard, W. A. The Two-Phase Model for Calculating Thermodynamic Properties of Liquids from Molecular Dynamics: Validation for the Phase Diagram of Lennard-Jones Fluids. *The Journal of Chemical Physics* **2003**, *119* (22), 11792–11805.